International Journal of Heat and Mass Transfer 152 (2020) 119569

Contents lists available at ScienceDirect

International Journal of Heat and Mass Transfer

journal homepage: www.elsevier.com/locate/hmt

Characterization and thermal modeling of a miniature silicon vapor chamber for die-level heat redistribution

Tanya Liu[a], Marc T. Dunham[b], Ki Wook Jung[a], Baoxing Chen[c], Mehdi Asheghi[a], Kenneth E. Goodson[a,*]

[a] Department of Mechanical Engineering, Stanford University, Stanford, CA 94305, United States
[b] Analog Devices, Inc., Santa Clara, CA, 95054, United States
[c] Analog Devices, Inc., Wilmington, MA, 01887, United States

ARTICLE INFO

Article history:
Received 13 November 2019
Revised 19 February 2020
Accepted 22 February 2020
Available online 6 March 2020

Keywords:
Vapor chamber
Heat spreader
Evaporation
Wick microstructures
Silicon

ABSTRACT

Vapor chambers are passive heat spreaders that can improve system level temperature uniformity through efficient heat transport in a high effective thermal conductivity vapor core. Fabricating a vapor chamber out of silicon is highly appealing due to the potential for direct integration schemes with existing semiconductor devices, but may be impractical from a cost perspective if the size of the vapor chamber must be much larger than the die. We investigate the potential benefit to using a miniature silicon vapor chamber with an active vapor transport region of 1 × 1 cm^2 for the purpose of die-level heat redistribution. Due to the high amount of liquid charging precision required for working with such small-scale vapor chambers, a reduced order thermo-fluidic model is developed to predict the effect of both heat flux and liquid charge on the overall device thermal performance. The model incorporates wick microstructure effects and is validated against experimental results from a prototype device to agree within ±25%. The thermal performance of the vapor chamber is benchmarked against simulation results for solid silicon spreaders of comparable dimensions and is found to improve the hotspot temperature uniformity at heat fluxes above 60 W/cm^2.

1. Introduction

As electronic systems continue to miniaturize in size and increase in overall power density, significant challenges arise in providing adequate thermal management to meet high performance metrics without impacting overall package size. Localized hotspots can generate heat fluxes on the order of 0.1 - 1 kW/cm^2 [1,2], often straining the limits of existing cooling technologies and necessitating an intermediary heat spreading layer before heat removal. Vapor chambers have been demonstrated in literature to be extremely effective heat spreaders with performance often exceeding that of solid spreaders due to the high effective thermal conductivity of the vapor transport in the core region [3–5]. Much research has been devoted to the study of copper vapor chambers, as copper has a high innate thermal conductivity and can be easily machined and processed [6–8]. Copper, however, is not coefficient of thermal expansion (CTE) matched to most semiconducting materials, requiring an extra layer of mechanically compliant thermal interface material between the die to be cooled and vapor chamber. The large temperature drop across these typically low thermal conductivity interface materials can often act as a thermal bottleneck for the entire system, particularly for higher power dies [9].

There is therefore great interest in developing silicon-based vapor chambers, as silicon is CTE compatible with many semiconducting materials and can be processed using standard microfabrication techniques. Vadakkan et al. performed mechanical simulations of a silicon die bonded to first a solid copper spreader and then a silicon vapor chamber, and found that the CTE matched silicon vapor chamber was able to reduce the stress in the die by up to 50% [10]. In addition to minimizing the stress on the die, a variety of potential integration strategies could be implemented with a silicon vapor chamber to reduce both the overall thermal resistance as well as form factor of the final package. For example, one cooling scheme could have the silicon evaporator wick structure fabricated directly on the die itself, similar to embedded microchannels where the cooling strategy is brought as close to the hotspot as possible. Another strategy could involve a silicon vapor chamber integrated into a traditional interposer design to add an additional layer of heat spreading. Much work in literature has been focused on the development of silicon micro heat pipe arrays, where small grooves with convex cusped cross sections can be

* Corresponding author.
E-mail address: goodson@stanford.edu (K.E. Goodson).

https://doi.org/10.1016/j.ijheatmasstransfer.2020.119569
0017-9310/

Nomenclature

A	area
d	Micropillar diameter
h	Micropillar height
h_{eff}	Effective condenser liquid height
k	Thermal conductivity
K	Permeability
m	Mass
M	Molar mass
n	Number of unit cells
p	Micropillar pitch
P	Pressure
q''	Heat flux
Q	Power
r	Radius
R	Thermal resistance
R_u	Universal gas constant
T	Temperature
U	Average unit cell cross sectional fluid velocity
V	Volume

Subscripts

act	Active device region
adv	Advancing
avg	Average
c	Condenser
cell	Unit cell property
ch	Charge
e	Evaporator
fg	Saturated vapor-liquid difference
hs	Hotspot
i	Unit cell index
inp	Input
int	Interface
l	Liquid
p	Pillar
s	Solid
sat	Saturated
side	Sidewall
tf	Thin-film
v	Vapor
vc	Vapor chamber
w	Wick

Greek symbols

α	Accommodation coefficient
β	Geometric fitting parameter
δ	Thin-film profile
κ	Curvature
θ	Contact angle
μ	Dynamic viscosity
ρ	Density
σ	Surface tension
υ	Specific volume
φ	Porosity

embedded directly into the die substrate [11–14]. These are typically designed for one-dimensional heat transport without any spreading effect, however, with a condenser portion located downstream of the evaporator. Fewer studies have focused on the development of silicon-based vapor chambers for heat spreading applications, where a larger area condenser and evaporator are located on opposite faces of the device. The dimensions of previous silicon vapor chambers in literature (in the range of 2×2 cm^2 to 5×5 cm^2) are typically much larger than a standard die size in order to reduce the heat flux to the condenser side as much as possible [15–20]. From a cost and packaging perspective, however, it may not always be feasible for manufacturers to implement a silicon vapor chamber much larger than the die. Silicon processing is often thought of in terms of cost per unit area, a factor that has stayed roughly constant over the past few decades [21]. Electrical constraints may also prevent multiple dies from being integrated with the same spreader without sufficient electrical insulation. As most electrical insulators are also thermal insulators, this would reintroduce unwanted thermal interfaces into the system and negate the advantage of an integrated silicon vapor chamber. We therefore investigate the potential benefit to overall system thermal management in implementing an integrated, die-area matched silicon vapor chamber.

In this paper, we present a miniature silicon vapor chamber with an active area of 1×1 cm^2 for the purpose of die-level heat redistribution. The vapor chamber is capillary-driven with silicon micropillar wicking structures that line both the condenser and evaporator surfaces. We develop a model to predict the effect of total liquid charge volume and heat flux on the overall device thermal resistance and validate against experimental results with a prototype device. The thermal performance of vapor chambers and heat pipes has been observed to be strongly dependent on the liquid charge volume [22–24], a factor that becomes even more critical when working with a miniaturized device with expected charge volume on the order of microliters. A standard approach to identify the ideal charge volume is to iterate experimentally. Full-scale numerical simulation of the conjugate, two-phase heat and mass transport within a vapor chamber is computationally expensive and can present minimal benefit over an experimental approach. Many models in literature also make the simplification of a saturated wick and cannot account for the effect of varying liquid charge on the overall thermal performance [25–29]. The assumption of a saturated wick neglects microscopic pore level effects on wick permeability and effective thermal conductivity, which can be significant depending on the geometry and heat flux level considered. Ranjan et al. developed a detailed conjugate simulation that coupled a wick microstructure model with a vapor chamber macro-model through an evaporative mass flux correction factor [30], and noted that accounting for microstructure effects is especially critical for wick thicknesses on the order of 100 μm or less. More work has been done in the area of modeling micro heat pipes, as accounting for the meniscus curvature in the heat pipe grooves is required to drive the liquid flow from the condenser to evaporator section [31, 32]. Do et al. developed a numerical model capable of predicting the effect of liquid charge on thermal resistance as well as maximum heat flux for a flat, grooved wick micro heat pipe [33]. Similar work, however, has not been extended to a two-dimensional capillary driven vapor chamber configuration such as the one considered in this paper. The goal of this paper is to therefore provide a model to predict the effect of liquid charge and heat flux on the thermal performance of a miniature vapor chamber, accounting for wick microstructure effects, without the need for a full conjugate numerical simulation. For a silicon vapor chamber to viably partake in a future die-integrated thermal management system, new electro-thermal oriented manufacturing processes need to be developed to ensure proper evacuation and charging of the chamber. The aim of the model is to provide overall guidelines that can be used to optimize future designs, and provide information on required process control tightness to increase the feasibility of implementing an integrated vapor chamber in an actual chip package. Additionally, the model can be used to assess the performance of the miniature vapor chamber in a variety of different system level configurations to create future design roadmaps.

2. Theory

We develop a reduced order thermo-fluidic model to predict the effect of both heat flux and liquid charge on the overall thermal resistance of the vapor chamber. The model does not attempt to calculate the operational limits of the device, thereby allowing the thermal resistance to be calculated from an equivalent solid conduction model without a full numerical simulation of the coupled flow and temperature fields [25]. The effective thermal conductivities of the condenser/evaporator wicks are dependent on the liquid distribution and temperature within the device, however, requiring still some knowledge of the fluid flow. Fluid flow sub-models are therefore developed for each region to account for wick microstructure effects and provide a more accurate estimate of the device resistance without the need for a full conjugate numerical simulation. Additionally, the fluid flow sub-models provide a means to track the total mass of working fluid within the vapor chamber, allowing the model to account for the effect of liquid charge volume. The following sections will go over the thermo-fluidic models for the evaporator wick, condenser wick, and overall model calculation flow.

2.1. Evaporator model

An overall cross-sectional schematic of the capillary wicked silicon vapor chamber considered in this work is shown in Fig. 1(a). Heat generated from a square hotspot on the evaporator side of the device causes the liquid within a square-packed micropillar wick to evaporate into vapor, which then spreads throughout the vapor core region before condensing back into liquid in the condenser wick. In the evaporator micropillar wick, evaporation from the centrally located heat source creates a non-uniform liquid distribution as shown in inset of Fig. 1(a). As the input heat flux increases, further recession of the liquid into the pores of the heated region increases the area for evaporation and reduces the overall wick resistance [34–37]. Therefore, to accurately capture the effective thermal conductivity as a function of heat flux and liquid charge, the model must be able to incorporate the effect of varying meniscus shape along the length of the evaporator wick. To account for this, we adapt the experimentally validated fluid flow model developed by Zhu et al. to solve for the liquid meniscus distribution along the wick as a function of input heat flux [34].

We extend their model to account for a non-uniform heat input and approximate the liquid flow as one-dimensional, radial flow from the edges of the wick towards the central heated region. As shown in Fig. 1(b), the actual flow field is not precisely radial due to the square geometry of the heated area and overall wick area. To enable the radial approximation, the square heated area is therefore converted to a circular area by defining an equivalent radius, r_{hs}, such that

$$r_{hs} = \sqrt{\frac{A_{hs}}{\pi}} \tag{1}$$

The square wick is similarly converted into a radial equivalent with the same method, then divided into an array of unit rings as shown in Fig. 1(b), where the rings are numbered such that $i = 0$ at the wick edge and increases monotonically towards the wick center. While this conversion leads to sections of rings that span

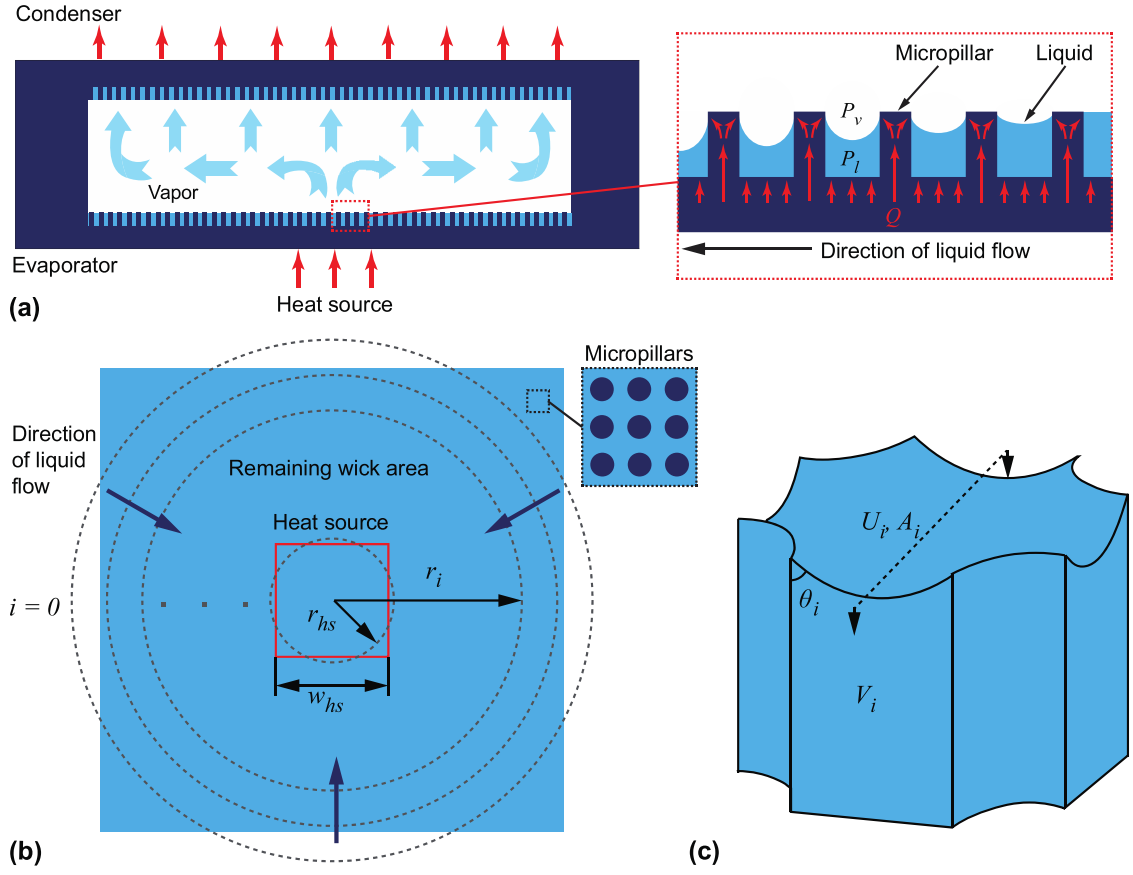

Fig. 1. (a) Cross-sectional schematic showing the general principles of the miniature silicon vapor chamber. Inset shows the variation in meniscus distribution and heat flux vectors in the evaporator wick. (b) Top view of radial representation of flow through evaporator wick. The wick is divided into a set of unit rings, with $i = 0$ starting at the edge of the wick. (c) Representation of a single unit cell within the ith unit ring. The cross sectional area, A_i, unit cell volume, V_i, and area-averaged velocity, U_i, are tabulated as a function of pressure drop across the unit cell for a range of different meniscus curvatures and apparent contact angles, θ_i.

outside of the physical device borders, it preserves the total areas of the heat source and wick and provides a more accurate accounting when calculating the total liquid charge contained within the wick. Each i^{th} unit ring is assumed to be comprised of a number of unit cells, n_i, equal to

$$n_i = \frac{2\pi r_i}{p_i} \tag{2}$$

where r_i is the radius of the i^{th} ring, and p_i is the pitch of the micropillars within that ring. The unit cells within each ring have a distinct meniscus shape that satisfies the Young-Laplace equation. The Young-Laplace equation describes the capillary pressure difference sustained across the liquid vapor interface, which can be written as

$$\Delta P_{lv} = P_v - P_l(r) = 2\sigma\kappa(r) \tag{3}$$

where P_v is the vapor pressure, P_l is the radially dependent liquid pressure, σ is the liquid-vapor surface tension, and κ is the radially dependent meniscus curvature. We assume that the radial gradient in vapor pressure is small compared to the liquid pressure gradient, as is typical in vapor chambers, such that P_v can be considered approximately constant.

Unique unit cell meniscus shapes are generated for a large range of vapor-liquid pressure differences using a force balance model in COMSOL, details of which can be found in [34]. The liquid is assumed to exist in a pinned state at the top of the micropillars, with a minimum sustainable contact angle equal to the receding contact angle for the working fluid and solid surface under consideration. The contact angle for each unit cell, θ_i, is defined as shown in Fig. 1(c) as the angle between the meniscus interface and the pillar surface. The difference in meniscus curvature from the unit cells within one ring to the next creates the capillary pressure difference that drives fluid flow from the wick outer edge to the central heated area. The average cross sectional area A, flow velocity U, and unit cell volume V are tabulated through computational fluid dynamics (CFD) simulations in COMSOL as functions of the liquid meniscus shape and pressure drop across the unit cell. Due to the tedious nature and large number of simulations required to create such reference tables, the working fluid properties for each simulation are held fixed at a reference point of 100 °C. When using water as the working fluid, the primary effect of this assumption is to underpredict the contact angle at temperatures below 100 °C due to the increase in surface tension with decreasing temperature. The effect of the underprediction is small, however, for the range of vapor liquid pressure differences considered in this paper (< 150 Pa). For example, the variation in predicted apparent contact angle for the pressure difference of $\Delta P_{lv} = 150$ Pa is only around 1.2% when using reference temperatures of 100 °C versus 50 °C. If the model were to be extended for the prediction of dryout heat flux, however, a potentially much larger pressure difference range would need to be considered, and temperature dependent meniscus shapes would need to be taken into account.

The total mass flux across each ring can be found through the summation of the mass flux through each unit cell. For non-circular packed arrangements of micropillars, this radial treatment will lead to an underprediction of the mass flux per unit cell near the wick center where the effective radius is of the same order as the micropillar pitch. The error in total mass balance for the square packed pillar arrays considered in this study, however, is still less than 2%. A mass and energy balance across each unit ring couples the capillary pressure and mass flux with neighboring rings such that

$$\rho(n_{c,i-1}A_{i-1}U_{i-1} - n_{c,i}A_iU_i)h_{fg} = q_i''\pi\left(r_{i-1}^2 - r_i^2\right) \tag{4}$$

where q'' represents the heat flux for each ring, and ρ and h_{fg} are the density and latent heat of vaporization of the working fluid, respectively. Setting the starting capillary pressure, ΔP_{lv}, and average fluid velocity, U, at $i = 0$ gives the boundary conditions at the wick edge and enables the solution of the full meniscus distribution across the wick. The starting capillary pressure boundary condition is linked with the condenser sub-model as described in the following section. The starting velocity is set based on the assumption that all the fluid being evaporated must enter at the wick edge. With knowledge of the meniscus distribution and total liquid volume contained in each unit ring, we can calculate the total mass of liquid within the evaporator wick, m_e, through a summation over all unit rings, and begin the procedure to solve for the effective thermal conductivity.

We use a thermal resistance network as shown in Fig. 2(a) to derive the effective thermal conductivity of a micropillar unit cell. For a base heated micropillar unit cell, heat travels in parallel through the solid micropillar and bulk liquid film. Due to the low thermal conductivity of the neighboring bulk liquid, we assume that the heat flow in the micropillar is essentially one-dimensional,

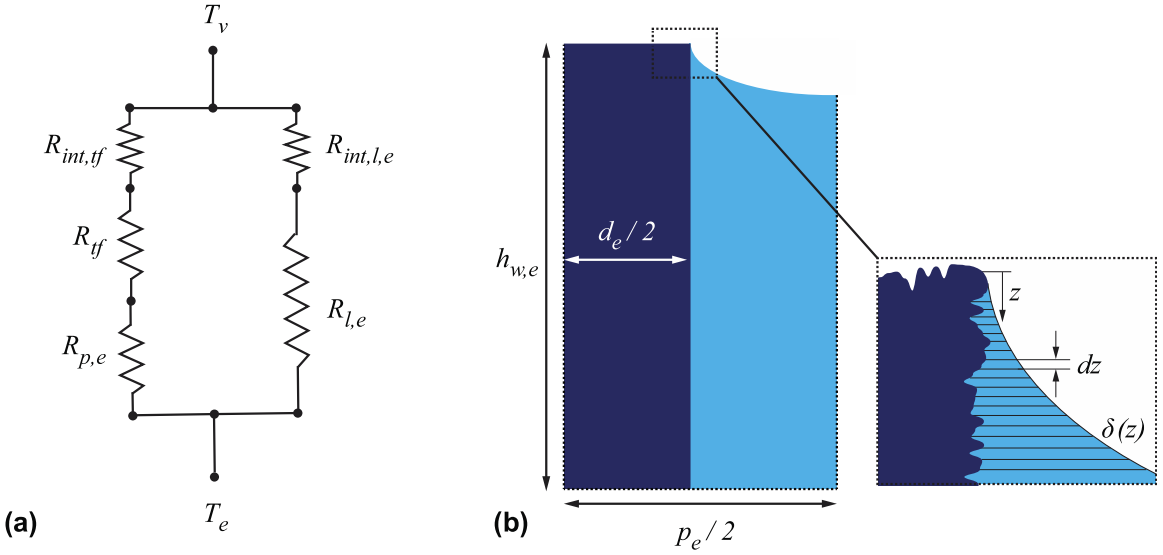

Fig. 2. (a) Resistance network for calculating the total thermal resistance across a micropillar unit cell in the evaporator wick. (b) Side view of evaporator wick with micropillar height $h_{w,e}$, pitch p_e, and diameter d_e. Inset shows a representation of the thin-film liquid profile, $\delta(z)$, where majority of evaporation occurs.

and the micropillar conduction resistance can be expressed as

$$R_{p,e} = \frac{h_{w,e}}{(1-\varphi_e)p_e{}^2 k_s} \tag{5}$$

where k_s is the thermal conductivity of the solid, and $h_{w,e}$, φ_e, and p_e represent the evaporator micropillar height, wick porosity, and pitch, respectively.

The bulk liquid conduction resistance is defined as

$$R_{l,e} = \frac{h_{w,e}}{\varphi_e p_e{}^2 k_l} \tag{6}$$

where k_l is the liquid thermal conductivity. For the combination of solid silicon and water as the bulk liquid, $R_{p,e} \ll R_{l,e}$, and the majority of the heat is expected to travel through the solid then evaporate from a microscale liquid film region along the top circumferential edge of the pillar. As the liquid meniscus in the evaporator wick becomes more concave, this thin liquid film area increases. For the range of microscale pore sizes considered here, various studies in literature have concluded that the thickness of this highly evaporative meniscus region (representing > 50% of the total evaporative heat transfer) ranges from approximately 1–10 μm [37–40]. This portion of the meniscus has been defined as the micro-region in some studies [38,40], however, various other studies on evaporation from microstructures have referred to this section of the meniscus as the thin-film region [35–37]. In this work, we refer to this highly evaporative region as the thin-film region, and define it as the portion of the meniscus with a liquid film thickness less than or equal to 5 μm. We neglect disjoining pressure effects on evaporation rate suppression as this has been shown to be insignificant for length scales > 100 μm [38,41], which is of the same order as the micropillar wick dimensions considered here.

For a given meniscus shape, we can estimate the thin-film area through integration of the meniscus curvature around the pillar surface. Due to the cylindrical pillar geometry under consideration, minimal variation of the thin-film profile is expected to occur around the pillar circumference. As shown in Fig. 2(b), the thin-film resistance is calculated through integration of the thin-film profile, $\delta(z)$. We treat each infinitesimal slice of the thin-film liquid profile as a parallel resistor with a thickness equal to $\delta(z)$ and area calculated from a surface of revolution approach. This leads to the following expression for the thin-film resistance R_{tf}, where

$$R_{tf} = \left[2k_l \pi \beta \int_0^{z_{tf}} \frac{\left(\delta + \frac{d_e}{2}\right)\sqrt{1+\left(\frac{d\delta}{dz}\right)^2}}{\delta} dz \right]^{-1} \tag{7}$$

z_{tf} is the distance from the micropillar top that marks the end of the thin-film region, d_e is the diameter of the evaporator micropillar, and β is a geometric fitting parameter that accounts for any enhancement in surface area that may occur from additional surface roughness on the micropillar, as well as additional thin-film evaporation that may be unaccounted for with the 5 μm film thickness assumption. The inset in Fig. 2(b) depicts an artistic rendering of an example micropillar surface texture. For micropillars fabricated through standard deep-reactive-ion-etching (DRIE) processes, β is expected to be close to 1. For micropillars that have undergone any additional surface treatment such as chemical etching, etc., β will be > 1.

The interfacial resistance is calculated using the Schrage equation [42] as

$$R_{int} = \frac{1}{A_{int}} \frac{2-\alpha}{2\alpha} \left(\frac{T_v \upsilon_{fg}}{h_{fg}{}^2}\right) \sqrt{\frac{2\pi R_u T_v}{M}} \left(1 - \frac{P_v \upsilon_{fg}}{2h_{fg}}\right)^{-1} \tag{8}$$

where A_{int} is the area of the interface, α is the accommodation coefficient, T_v is the vapor temperature, v_{fg} is the vapor-liquid specific volume difference, M is the molar mass of the working fluid, and R_u is the universal gas constant. The accommodation coefficient α is chosen as 0.1 in this work, on the same order as previously reported experimental values for evaporation of water from micropillars into a vapor saturated environment [36]. Note that the interfacial resistance is calculated separately for the thin-film and bulk liquid regions due to an expected variation in interfacial temperature along the meniscus. A non-isothermal interface may lead to the formation of thermocapillary vortices from Marangoni convection [43], though this effect has been reported to be small for the typical superheat range expected in a vapor chamber wick pore (< 5 °C) [41] and is neglected to preserve model simplicity.

The final expression for the unit cell effective thermal resistance is

$$R_{cell} = \left(\left(R_{p,e} + R_{tf} + R_{int,tf}\right)^{-1} + \left(R_{l,e} + R_{int,l,e}{}^{-1}\right)^{-1} \right)^{-1} \tag{9}$$

The equivalent resistance for the entire wick can then be expressed as

$$R_{w,e} = \left(\sum_{i=1}^{n_e} R_{cell,i}{}^{-1} \right)^{-1} \tag{10}$$

where n_e is the number density of unit cells in the evaporator wick. Finally, the equivalent resistance is converted into an effective thermal conductivity for use in the solid conduction model as

$$k_{w,e} = \frac{h_{w,e}}{R_{w,e} A_e} \tag{11}$$

2.2. Condenser model

Unlike the evaporator region of the device, we approximate the condenser region with a uniform vapor mass flux [5] due to the highly efficient nature of vapor transport and spreading in the core. This assumption applies as long as the pressure drop in the vapor core is minimal, as addressed in the following section. Condensation is expected to occur throughout the entire wick area, including the micropillar top surfaces and bulk liquid. This provides one of the primary advantages of a condenser side wick, which is to create a more uniform heat removal surface. In the absence of a wick structure, the formation of a bulk liquid film would introduce additional thermal resistance into the system. Other methods of potentially addressing this issue include chemical treatment to induce dropwise condensation on wickless hydrophobic condensers, or active droplet jumping on a superhydrophobic structured condenser [44].

For a superhydrophillic wick surface, we assume that the majority of liquid condensed on the pillar tops will wick into the liquid bulk. We relax the requirement of pinned liquid menisci at the micropillar top edges, and allow for the fact that for charge volumes with a total wick saturation ratio less than 1, the liquid in the condenser may not fill the wick to the full height of the condenser pillars. Additionally, if the condenser wick has a higher porosity than that of the evaporator wick, it would be energetically unfavorable for extremely concave, pinned meniscus shapes to form at the condenser side. We acknowledge that for low amounts of liquid charge volume, intermediary menisci states may also exist within the evaporator wick that are not necessarily pinned at the micropillar top edges, particularly if the micropillar surface is rough. The inclusion of these states would improve the accuracy of the model for low liquid charge volumes or near dryout heat fluxes, but would require additional computation beyond the scope of the current work. By assuming a pinned evaporator wick and unpinned condenser wick, we provide a system constraint to track the liquid redistribution within the device. We assume that in the event of overcharging, the entire condenser wick may become flooded and

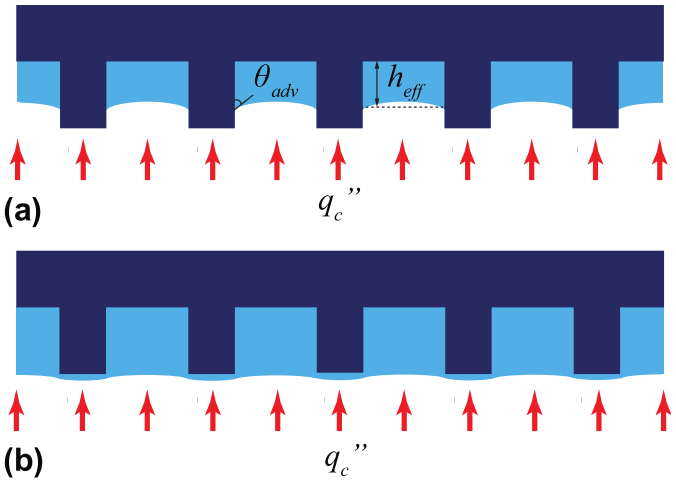

Fig. 3. Schematics of liquid distribution for two cases of liquid volume. (a) Model of condenser liquid distribution without flooding. (b) Condenser liquid distribution in the event of flooding, where a thin film forms on top of the micropillars and creates extra thermal resistance.

additional liquid condensate will form a steady film on the micropillar top surfaces. In reality, if the device is overcharged, the evaporator wick may flood as well. However, as the applied heat flux increases, the liquid will eventually redistribute to the condenser side. We therefore assume in the model that significant liquid redistribution will only occur on the condenser side, and the two different liquid distribution scenarios are depicted in Fig. 3.

In the case of a non-flooded wick as shown in Fig. 3(a), the fluid flow in the condenser can be approximated with an effective medium approach through the implementation of Darcy's law with a uniform condensation mass flux. We assume minimal variation in meniscus curvature throughout the length of the wick and approximate using an average meniscus contact angle, θ_{adv}, equal to the advancing contact angle. The value of θ_{adv} for water on SiO_2 is approximately 70° [45]. The permeability of the wick can be calculated through an analytical expression derived by Byon et al. for a fixed contact angle as

$$K_c = K_{2D}\left[1 - \frac{\exp\left(2\sqrt{\frac{\varphi_c}{K_{2D}}}h_{eff}\right) - 1}{\sqrt{\frac{\varphi_c}{K_{2D}}}h_{eff}\left(\exp\left(2\sqrt{\frac{\varphi_c}{K_{2D}}}h_{eff}\right) + 1\right)}\right] \tag{12}$$

where K_{2D} is the permeability for the micropillar array without meniscus effects, φ_c is the porosity of the condenser wick, and h_{eff} is the effective height of liquid in the wick that accounts for a uniformly curved meniscus while conserving the total liquid volume [46]. A detailed expression for K_{2D} is provided in the supporting information (SI) as well as [46]. The effective liquid height, h_{eff} is expected to vary with heat flux and liquid charge amount, and is calculated iteratively through the procedure described in Section 2.5. The final equation for the capillary pressure at the outer edge of the condenser wick in terms of the condenser side heat flux, q''_c, is

$$\Delta P_{lv,c} = \frac{q''_c \mu}{4\rho_l h_{fg} h_{eff} K_c} {r_c}^2 \tag{13}$$

where r_c is the equivalent radius of the wick edge, and we have assumed that the wet point of the vapor chamber where the liquid pressure is equal to the vapor pressure occurs at the very center of the condenser wick [30]. The detailed derivation of Eq. (13) is given in Section 1 of the SI. Eq. (13) then provides the boundary condition for the starting capillary pressure at the outer edge of the evaporator wick, effectively coupling the liquid flow in the two portions. When the condenser is in the flooded scenario (Fig. 3(b)), we treat the condenser as a liquid reservoir for flow to the evaporator and set the starting capillary pressure boundary condition equal to zero.

Since vapor is condensed over the entire wick area, the effective thermal conductivity of the condenser can be calculated by treating the solid micropillar and liquid bulk resistances in parallel. The solid micropillar and liquid bulk resistances are calculated in a similar manner to the evaporator wick, and the exact expressions are not repeated again for brevity. The final expression for the effective condenser thermal conductivity is thus

$$k_{w,c} = \frac{h_{w,c} + \Delta h}{\left({R_{p,c}}^{-1} + {R_{l,c}}^{-1}\right)^{-1} A_c} \tag{14}$$

where

$$\Delta h = \begin{cases} 0, & h_{eff} \le h_{w,c} \\ h_{eff} - h_{w,c}, & h_{eff} > h_{w,c} \end{cases}$$

and the interfacial resistance across the bulk liquid-vapor interface based on Eq. (8) has been lumped into $R_{l,c}$.

2.3. Vapor core model

Due to the relatively thick vapor core and small vapor spreading distance (675 μm and ~5 mm, respectively) considered in our miniature vapor chamber, the pressure drop and subsequent temperature drop in the vapor core are expected to be insignificant compared to the wick regions. The vapor core can thus be modeled as a block with very high thermal conductivity. A previous study reported an effective vapor core conductivity of 23,000 $Wm^{-1}K^{-1}$ for a vapor chamber with a vapor core thickness comparable to our device (635 μm) and significantly longer vapor spreading distance (~ 45 mm) [25]. We choose a conservative value of k_v = 20,000 $Wm^{-1}K^{-1}$ for the remainder of our model calculations to serve as a lower bound to the vapor core conductivity. The model is not sensitive to the exact value of k_v, as the thermal resistance of the vapor core is negligible compared to the effective wick resistances. Note that this assumption will no longer be appropriate if the spreading distance increases significantly or the core becomes drastically thinner. For ultra-thin vapor chambers with core thicknesses on the order of 100 μm, the vapor resistance is expected to dominate the system performance, and additional calculations are needed to accurately account for the effective vapor core conductivity and pressure drop [47].

2.4. Solid conduction model

Since the effective thermal conductivities of the evaporator and condenser wicks are functions of heat flux, it is important to characterize any parallel heat flow that may occur outside of the active phase change region of the device. This will be particularly significant for cases where flooding of the condenser wick may occur and create higher resistance states that cause more heat flow to be diverted elsewhere. We therefore estimate the active power contributing to evaporation/condensation within the porous wicks by accounting for two parallel heat transfer pathways, one flowing through the active vapor chamber region where phase change occurs, Q_{act}, and another flowing through the bonded solid sidewalls that form the periphery of the active vapor chamber region, Q_{side}. We estimate the sidewall conduction resistance, R_{side}, to be approximately 8.2 °C/W by performing a finite element simulation in COMSOL on a dry vapor chamber with no working fluid. To calculate Q_{act}, we estimate the resistance of the active vapor chamber region, R_{act}, based on the geometry as shown in Fig. 4(a) where the evaporator wick, condenser wick, and vapor core thermal conductivities are calculated from the sub-models described

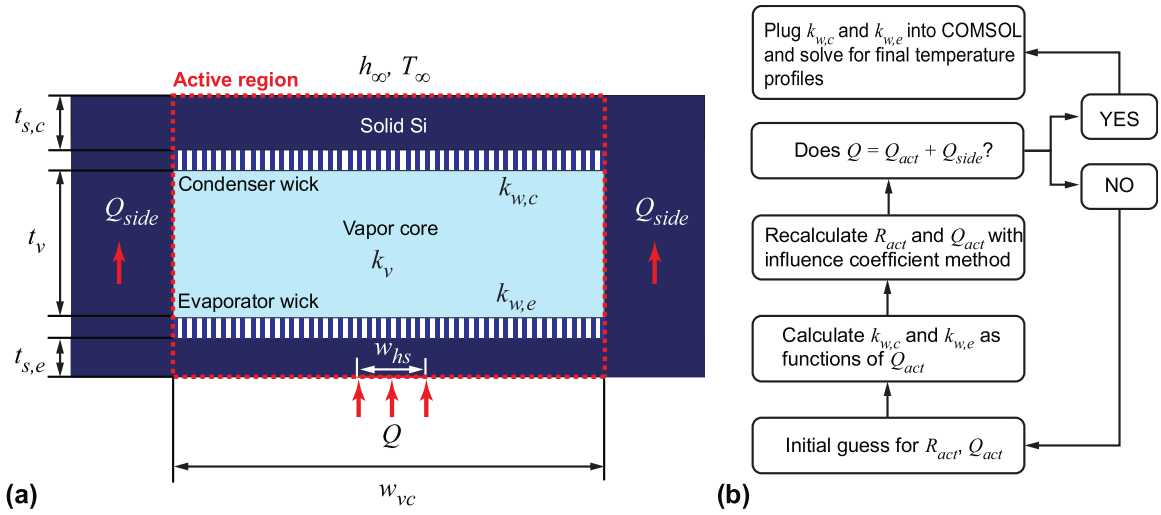

Fig. 4. (a) Schematic outlining the heat flow pathways and relevant geometric parameters in the vapor chamber, where the total heat flow, Q, is split between the active region where phase change occurs, and parasitic heat flow through the bonded sidewalls. (b) Flow chart showing calculation procedure to estimate active heat flow and heat flux dependent wick thermal conductivities. An initial guess is made for R_{act} and Q_{act}, then updated until an energy balance is satisfied.

in the previous sections, and the remainder of the vapor chamber stack is composed of solid silicon. To facilitate rapid iteration and incorporation of the sub-models on the same computing platform, an estimate of R_{act} is obtained for the active region geometry in Fig. 4(a) by using the analytical influence coefficient method developed by Muzychka [48]. The details of the sidewall conduction resistance simulation and implementation of the influence coefficient method are given in Section 2 of the SI. Finally, Q_{act} can be calculated from the relative resistance ratio of R_{side} and R_{act}, and the effective evaporator and condenser wick thermal conductivities as functions of Q_{act} are input into a solid conduction simulation in COMSOL to obtain the complete, three-dimensional temperature distribution within the vapor chamber. The total device resistance can then be calculated as

$$R_{vc} = \frac{T_{hs,avg} - T_{c,avg}}{Q} \tag{15}$$

where $T_{hs,avg}$ and $T_{c,avg}$ are the average hotspot and condenser temperatures, respectively. The model flow to calculate $k_{w,c}$ and $k_{w,e}$ as functions of Q_{act} is shown in Fig. 4(b).

2.5. Model calculation procedure

The overall system of equations for the evaporator/condenser wick sub-models and analytical influence coefficient model are programmed in MATLAB. Temperature dependent thermophysical properties of the working fluid are computed at each step based on tabulated values in literature using the average vapor temperature of the system, or $T_{v,avg}$ [49]. The general model calculation flow to find the vapor chamber thermal resistance as a function of total heat input, Q, and liquid charge mass, m_{ch}, is as follows:

1 Initialize a guess for the average vapor temperature, $T_{v,avg}$, condenser side liquid film thickness, h_{eff}, and active vapor chamber resistance, R_{act}.
2 Solve the condenser wick sub-model for $\Delta P_{lv,c}$, $k_{w,c}$, and m_c as functions of Q_{act}, h_{eff}, and $T_{v,avg}$.
3 Using the results from the condenser sub-model, set $\Delta P_{lv,c}$ as the boundary condition at $i = 0$ for the evaporator wick sub-model, solve for $k_{w,e}$ and m_e as functions of Q_{act} and $T_{v,avg}$.
4 Calculate the mass of vapor, m_v by treating it as an ideal gas with temperature and pressure equal to $T_{v,avg}$ and $P_{v,avg} = P_{sat}(T_{v,avg})$
5 Using $k_{w,c}$, $k_{w,e}$ and k_v as inputs to the analytical influence coefficient model, solve for an updated guess on $T_{v,avg}$ and R_{act} for heat input Q_{act}.
6 Check if $m_e + m_c + m_v = m_{ch}$ ±1% and $Q_{act} + Q_{side} = Q \pm 1\%$. If not, repeat steps 1–5 until the tolerance is met.
7 Plug in $k_{w,c}$ and $k_{w,e}$ to COMSOL for a final calculation of the temperature distribution.

3. Experimental methods

3.1. Device geometry and fabrication

Fig. 5(a) shows the overall fabrication process flow for the miniature silicon vapor chamber. The active vapor chamber area of the device is 1 × 1 cm^2, with a total vapor chamber thickness of 1.5 mm. 5 mm of solid silicon is included around the periphery of the active vapor core area to allow space for bonding and patterning of electrical contact pads for a thin-film heater and resistance temperature detectors (RTDs). A 1 mm thick, 4 inch silicon wafer is used for the evaporator side in order to account for the vapor core cavity thickness, and a 500 μm thick, 4 inch wafer is used for the condenser side with no vapor core cavity. Both wafers go through an initial thermal oxidation step to grow approximately 400 nm of SiO_2 for electrical passivation. Standard photo-lithography techniques are used to expose, develop, and pattern 100 nm of platinum with a 10 nm chromium adhesion layer for the heater and RTDs. The electrical heater and RTD mask layouts for both the evaporator and condenser sides of the device are shown in Fig. 5(b) and (c). On the evaporator side, a serpentine heater over a 3.2 × 3.2 mm^2 area represents the heat source from the die, and 7 different RTDs (labeled as T_{E1-7} in Fig. 5(b)) are distributed across the 10 × 10 mm^2 active evaporator area as well as interspersed between the serpentine heating lines to measure the temperature distribution across the entire evaporator/hotspot for various heat inputs. The average hotspot temperature used in the thermal resistance calculation is estimated by taking the average of T_{E7}, T_{E6}, and T_{E3}. The condenser side has 9 RTDs located at various points across the condenser area to similarly provide information about the condenser side temperature distribution as a function of heat input. Due to microfabrication defects, only 5 of the patterned RTDs were functional on the condenser side ($T_{C1\text{-}4}$ and T_{C6}). The average condenser temperature is calculated from the average of measurements obtained from T_{C1}, T_{C2}, T_{C4} and T_{C6}. No central tem-

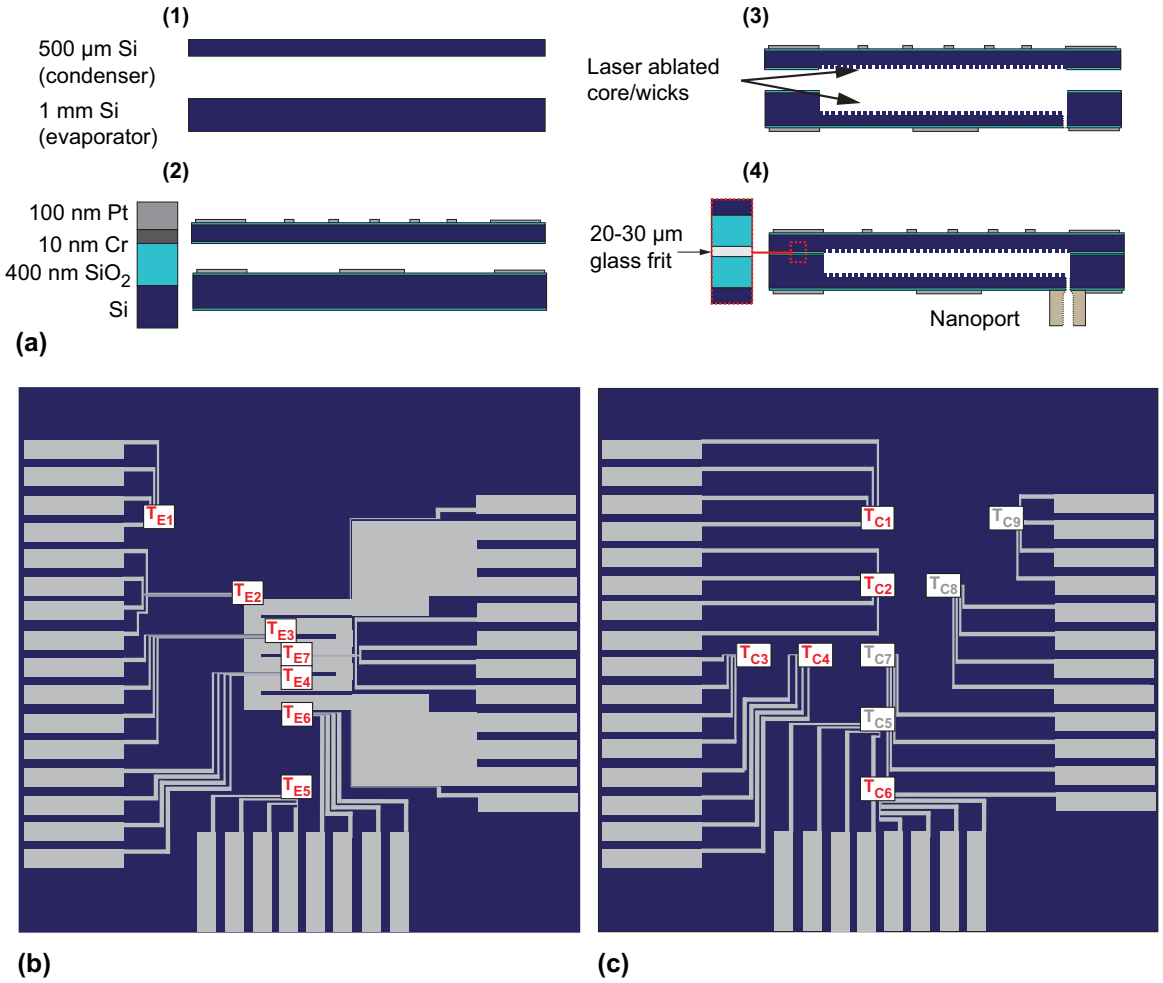

Fig. 5. (a) Fabrication process flow for condenser and evaporator sides starting from (1) 500 μm thick and 1 mm thick substrates for condenser and evaporator sides, respectively (2) thermal oxidation, then photolithography and metal evaporation to define heater and RTDs, (3) laser ablation to etch vapor core, wick structures, and through-hole, (4) glass frit bond and Nanoport attachment. (b) Evaporator side heater and RTD layout. (c) Condenser side RTD layout. Due to microfabrication defects, only $T_{C1\text{-}4}$, and T_{C6} were functional.

perature measurement was available on the condenser side, but the resulting error in the average temperature is expected to be minimal due to the high thermal conductivity of the vapor core. Measurements from a separate, identically fabricated device with a functional central RTD showed a less than 1% difference between an average condenser temperature calculated with and without the central RTD measurement.

After patterning the heater and RTDs, the vapor core and evaporator/condenser wick structures are fabricated through ultra-violet (UV) laser ablation with a pulsed neodymium-doped yttrium orthovanadate (Nd/YVO4) laser (Samurai UV Laser Marking System from DPSS (Diode Pumped Solid State) Lasers Inc). Laser ablation is chosen over standard DRIE processes to avoid the complexity of performing a two-step etch process to define both the vapor core and wick structure in a single wafer. While the use of laser ablation limits the minimum feature size achievable to around 70 μm, deep etch features such as the vapor core can be performed with relative ease. Additionally, the laser ablation generates a conformal microscale roughness on the etched features that increases the surface area for heat transfer and promotes superhydrophilicity, potentially providing a pathway for performance enhancement over smooth, traditionally microfabricated surfaces. Fig. 6(a) depicts a scanning electron micrograph (SEM) of a laser-ablated micropillar, with distinct surface roughness generated on the pillar sidewall as well as pillar base (Fig. 6(b)). The laser ablation process results in

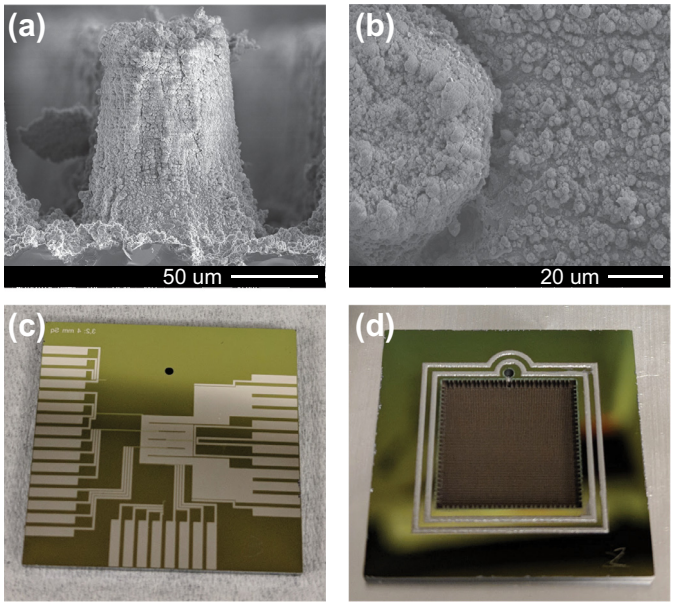

Fig. 6. (a) Sideview of micropillar fabricated through laser ablation. (b) Top view close up of microscale roughness generated on micropillar wick structures from laser ablation. (c) Evaporator side device with patterned heater/RTDs and through-hole. (d) Glass frit pattern after initial glazing step.

Table 1
Approximate dimensions versus model values for the silicon vapor chamber studied in this work.

Dimension	w_{vc} [mm]	w_{hs} [mm]	$t_{s,c}$ [μm]	$t_{w,c}$ [μm]	t_v [μm]	$t_{w,e}$ [μm]	$t_{s,e}$ [μm]
Actual Value	10	3.16	394±17	106±17	679±44	110±7	321±51
Model value	10	3.16	400	100	675	100	325

slightly conical pillars due to the change in laser focus plane as more material is ablated away. The wick structures on both the evaporator and condenser sides of the vapor chamber are square packed cylindrical pillar arrays, linked by perpendicular grooves around the periphery of the vapor cavity for condensate return. A through-hole, visible in Fig. 6(c), is also defined for each device during the etching process on the evaporator side to serve as a port for evacuation and liquid charging.

After defining the vapor core and wick structures, the devices are sonicated for 20 s to remove any accumulated silicon debris from the ablation process. The evaporator and condenser sides are then joined together with a glass frit bond (Koartan 5645-Si sealing glass paste). The frit includes organic binders mixed in with glass particles that must be burned out first during a high temperature (~ 450 °C) glazing step, otherwise incomplete binder burnout will lead to a weak bond with potential outgassing and generation of non-condensable gases during the device operation. The printed glass frit sealing rings after the initial glazing step can be seen in Fig. 6(d). In order to perform parametric liquid charging experiments without the added uncertainty of device variation, a non-permanent and reusable connection is used to link the vapor chamber with external fluid lines through a microfluidic Nanoport (Idex HS). A leak-tight connection is formed between the Nanoport and silicon surface through an o-ring face seal, and epoxy is applied to maintain the compressive sealing force. The Nanoport was chosen mainly for experimental convenience, and other methods to form more robust and permanent connections for future devices could involve soldering metal tubing to a metalized port [15], or performing the device bond step in a saturated environment [12].

The approximate physical dimensions of the vapor chamber versus dimensions used in the model are tabulated in Table 1. For model simplicity and due to the relatively imprecise nature of the laser machining process, we approximate both the condenser side and evaporator side wicks as consisting of 100 μm tall, perfectly cylindrical pillars. The estimated difference in fully saturated wick liquid volume using the measured versus approximate model values is less than 6% when taking into account the conical shape of the fabricated pillars. Additionally, the serpentine heater is approximated as a uniform heat source in the evaporator wick model to simplify the unit cell calculations. To ensure that this assumption does not significantly impact model results, the solid conduction model was run for the case of 11.9 μL liquid charge volume with both heating distributions. The predicted values for the temperature distribution at the RTD measurement locations varied by less than 1.3% when using a uniform heater versus the serpentine pattern. Based on these results, we concluded that the serpentine heat source can be reasonably represented by a uniform heat source, as sufficient heat spreading occurs in the solid silicon in between the patterned heating lines.

3.2. Experimental set up

A custom electrical connector was designed and fabricated in order to power the evaporator side heater and collect measurements from the thin-film RTDs on both sides of the device. To avoid the tedious process of wirebonding a double-sided device, two arrays of spring-loaded pogo pins mounted in PEEK are used to electrically connect to either side of the vapor chamber in a sandwich configuration. A four-wire configuration is used for each of the RTDs and the serpentine heater to eliminate the issue of contact resistance between the pogo pins and patterned metal surface. One side of the pogo connector with no vapor chamber present is shown in Fig. 7(a). The pogo pins are visible as the gold colored protrusions lining the center of the connector. An open window is purposefully left in the connector on both sides to allow for connection to a condenser side cooling mechanism and thermal insulation of the evaporator side. Fig. 7(b) shows the fully assembled doubled-sided connector configuration with the evaporator side of the vapor chamber facing up. A detailed cross sectional view of the various components comprising the connectors is given in Fig. 7(c). A miniature copper microchannel cold plate was designed for heat removal from the condenser side. To minimize parasitic heat loss through the non-active, solid bonding area of the vapor chamber, the contact area between the cold plate and vapor chamber was limited to only the 1×1 cm^2 active area of the vapor chamber through the use of a precisely sized thermal pad (Fujipoly). The temperature of the water supplied to the cold plate is maintained at 20 °C by an external chiller (Neslab RTE 7). Fig. 7(d) shows the cold plate assembled with the electrical connectors and vapor chamber (hidden from view).

During the heat transfer experiments, power is supplied to the evaporator heater in steady increments through a DC power supply (BK precision 9206). A 5 mm layer of silicone insulation is mounted on top of the evaporator side of the vapor chamber to prevent excessive heat loss to the environment. The voltage across the heater and resistances of the RTDs are monitored using a switching multimeter (Keithley DAQ 6510). Steady state is defined as the time at which the measured temperatures change at a rate of less than 0.05 °C/min over a 5-min period. The RTDs are calibrated prior to the experiment by submerging the entire electrical assembly into a heated liquid bath and creating calibration curves for resistance versus temperature. A T-type thermocouple is attached to each side of the device, and the difference between the temperature readings from the two thermocouples is less than 0.3 °C at each bath set point, within the given accuracy range for Omega special limits of error T-type thermocouples of ±0.5 °C. This reference thermocouple uncertainty dominates the experimental uncertainty in absolute temperature and thermal resistance. We estimate the heat loss from the device to the environment to be approximately 4% by running a finite element simulation in COMSOL with approximate system parameter values to account for natural convection to the environment and parasitic conduction through the solid silicon sidewalls. Further details of the calculation can be found in Section 3 of the SI. The reported heat flux values, q'', in the following sections represent the measured input heat flux, q_{inp}'', adjusted for 4% heat loss, with minimal error bars due to the high accuracy of the voltage and current measurements across the heater. The error bars reported for thermal resistance represent standard propagation of error incorporating the uncertainties in the steady-state temperature average and RTD calibration curves calculated for 95% confidence intervals.

3.3. Liquid charging and degassing procedures

A careful liquid charging and degassing procedure is followed prior to each heat transfer experiment. Water is chosen as the working fluid, and an initial estimate of the liquid charging amount assuming fully saturated evaporator and condenser wicks is on the

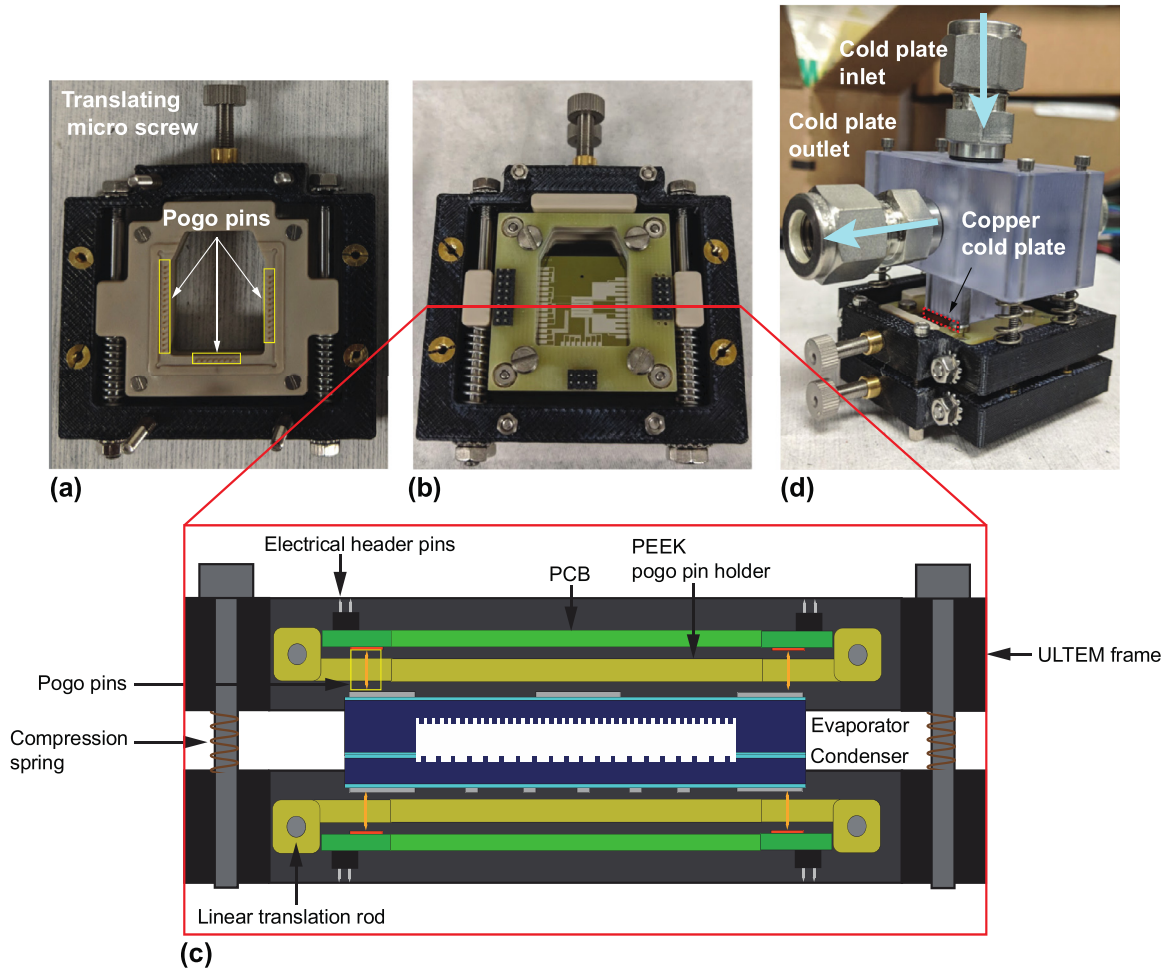

Fig. 7. (a) Single side of electrical connector with pogo pins exposed. (b) Electrical connector assembled with vapor chamber sandwiched in between. (c) Cross sectional schematic of assembled electrical connector in (b). Each connector consists of a PEEK pogo pin holder mated to a custom PCB to facilitate connections from the pogo pins to external measurement equipment. Once pins are precisely aligned, both connectors are compressed to make the electrical connections with the vapor chamber heater and RTDs. (d) Cold plate assembled on top of condenser side of vapor chamber.

order of 16 μL. Keeping track of the injected liquid amount post evacuation of the chamber using a flow meter or volume accumulator leads to a large uncertainty in the final liquid charge, as the dead volume associated with such devices is often comparable to the total desired liquid charge volume. Therefore, we charge the device first with deionized, ultra-filtered water using a syringe pump (Harvard Apparatus PHD 2000), and record the mass of the device before and after using a precision scale (Denver Instruments PI-225D) with 0.01 mg resolution for a more accurate measurement of the liquid charge.

The charged device is then connected to a vacuum line to remove the non-condensable gases within the chamber. Details of the evacuation set up components are given in Section 4 of the SI. A primary vacuum is performed first, in which the cold plate fluid temperature is set to 20 °C, and a vacuum is pulled until a quasi-steady pressure transducer reading of approximately 2.3 kPa is reached that corresponds to the saturation pressure of water at 20 °C. To prevent excessive loss of working fluid, a 2-way valve is closed periodically between the pump and charged device while the pressure reading is allowed to reach a quasi-steady state. Once the primary vacuum set point is reached, the device is closed to the vacuum pump, and a moderate heat flux of 5 W/cm^2 is applied to the evaporator heater. The chiller temperature is raised to 40 °C, and device is powered for one hour in this condition, then powered off and cooled back down to the chiller set point of 20 °C, where a brief secondary vacuum is performed to remove any non-condensable gases that may have been dissolved in the liquid charge. Experiments showed that further secondary vacuums with a higher chiller temperature had a negligible effect on the device thermal resistance, and thus the vacuum procedure was deemed sufficient to remove the majority of non-condensable gases within the chamber. Boreyko et al. used a similar fill and evacuation procedure for their vapor chamber and demonstrated effective removal of non-condensable gases through the primary and secondary vacuum steps [44]. A small amount of working fluid is lost after each experiment due to the evacuation procedure, but this is measured to be on average 1.5 μL or less through careful control of the evacuation time for each experiment. The hermeticity of the vapor chamber was tested by injecting the device with 13 μL of water, closing the Nanoport opening with a plug, and placing the entire chamber inside a vacuum dessicator for 380 h. The mass of the device measured before and after the vacuum dessication remained unchanged within 0.01%.

4. Experimental results and model validation

To verify the model, the thermal performance of the miniature silicon vapor chamber was characterized as both a function of heat flux and liquid charge following the experimental procedures detailed in the previous section. To preserve the device integrity for

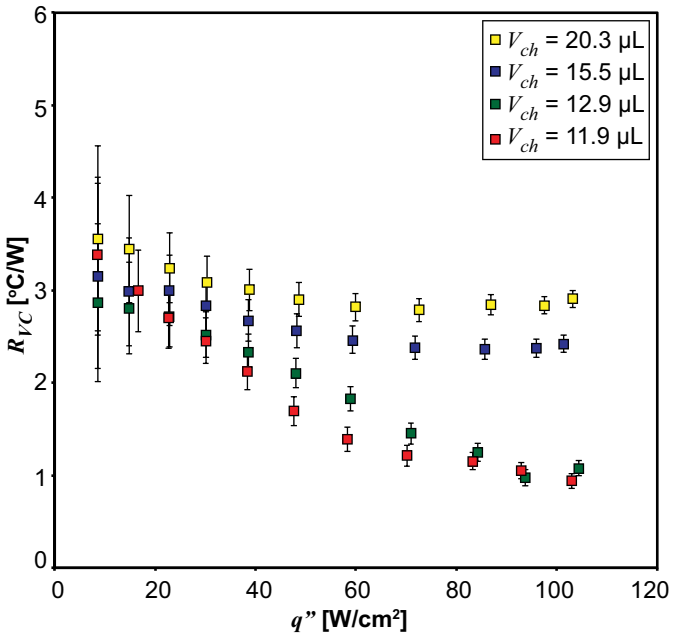

Fig. 8. Vapor chamber thermal resistance, R_{vc}, versus heat flux for different liquid charge volumes ranging from 11.9 μL to 20.3 μL. The resistance decreases with increasing heat flux for all liquid charge volumes. Increasing the liquid charge from 11.9 μL to 20.3 μL at the highest heat flux level considered of approximately 103 W/cm^2 increases the resistance by more than 300%.

repeated liquid charge experiments, the maximum heat flux was limited in each case to approximately 103 W/cm^2 to avoid any sudden temperature overshoot. The maximum operational heat flux of the device may be higher, though that limit was not explored in this work since the primary aim was prediction of thermal resistance. Fig. 8 shows the thermal resistance of the vapor chamber as defined by Eq. (15) as a function of heat flux for a range of liquid charge volumes from 11.9 μL - 20.3 μL. The relatively high uncertainty values at low heat fluxes are due to the fact that the measured temperature differences are close to the uncertainty of the temperature sensors (approximately ±0.6 °C). The thermal resistance of the vapor chamber noticeably decreases with decreasing liquid charge and increasing heat flux. At the maximum heat flux considered of approximately 103 W/cm^2, increasing the injected volume from 11.9 μL to 20.3 μL increases the resistance by more than 300%. The resistance behavior of the device is similar for the two lower charge volumes of 11.9 μL and 12.9 μL, but a clear transition occurs when the charge volume is increased to 15.5 μL.

Fig. 9(a) shows the model prediction against experimental results for the liquid charge volume of 12.9 μL with a range of different values for β, the fitting parameter to describe the enhancement in micropillar surface area due to the roughness generated from laser ablation. The experimental best fit is for $\beta = 3$, representing an approximately 3x enhancement in the laser ablated micropillar surface area over perfectly smooth pillars. We obtain a separate measurement of the roughened micropillar surface area enhancement over a smooth surface using a 3D laser scanning confocal microscope (Keyence VK-X Series) with 120 nm lateral and 500 nm vertical resolution. The laser microscope scans the surface using 408 nm violet laser light and measures the reflected laser light to create a detailed 3D depth map of the object of interest. A direct surface area measurement of the micropillar sidewalls is difficult due to the underlying curvature of the cylindrical micropillar. Therefore, we measure instead the surface area enhancement of the sidewalls that form the vapor core cavity, which have relatively flat surfaces and are created during the same ablation process as the micropillars. An example line profile showing the roughness over a small area of the vapor core sidewall obtained using the laser microscope is shown in Fig. 9(b). The average value for β returned by the microscope using an area scan over various portions of the sidewall is 8.3±3.3, the same order of magnitude as the model best fit. To provide another estimate, we also model the surface roughness based on the approximate values generated by the line profile as a uniform coating of 2 μm diameter pillars with 5 μm pitch and 3 μm height, which gives a lower bound of $\beta = 1.8$. The experimental best-fit value of $\beta = 3$ therefore seems a reasonable value and is used in all subsequent model calculations.

Fig. 10(a) shows the experimental temperature profiles plotted against model results for RTDs T_{E7}, T_{E6}, and T_{E5} on the evaporator side of the vapor chamber. The model shows fairly good agreement with the experimental profiles for T_{E6} and T_{E5}, but overpredicts the temperature rise for T_{E7} at higher heat fluxes. This may be due to the fact that the model calculates an area averaged thermal conductivity for the evaporator wick by treating all of the micropillar unit cells in parallel, when in fact the local resistance near the center of the wick may be lower due to increased curvature of the meniscus. For a more exact treatment, it may be appropriate to extend the model to account for anisotropy in the effective wick ther-

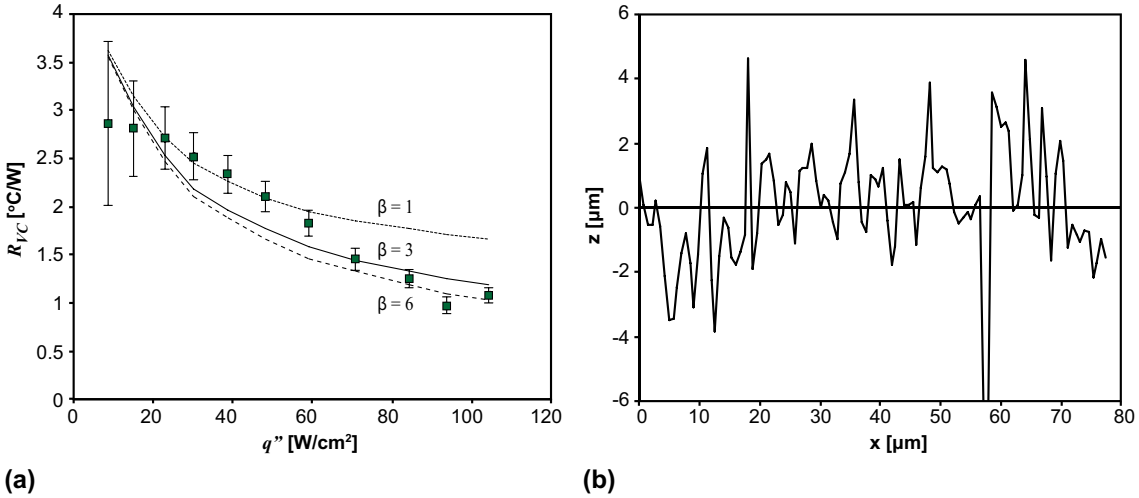

Fig. 9. (a) Model fit against experimental data for 12.9 μL charge volume for β, surface area enhancement factor due to the roughness of the laser ablated micropillars. Best fit against experimental results is for $\beta = 3$. (b) Laser scanning line profile of surface roughness measured from vapor chamber sidewalls.

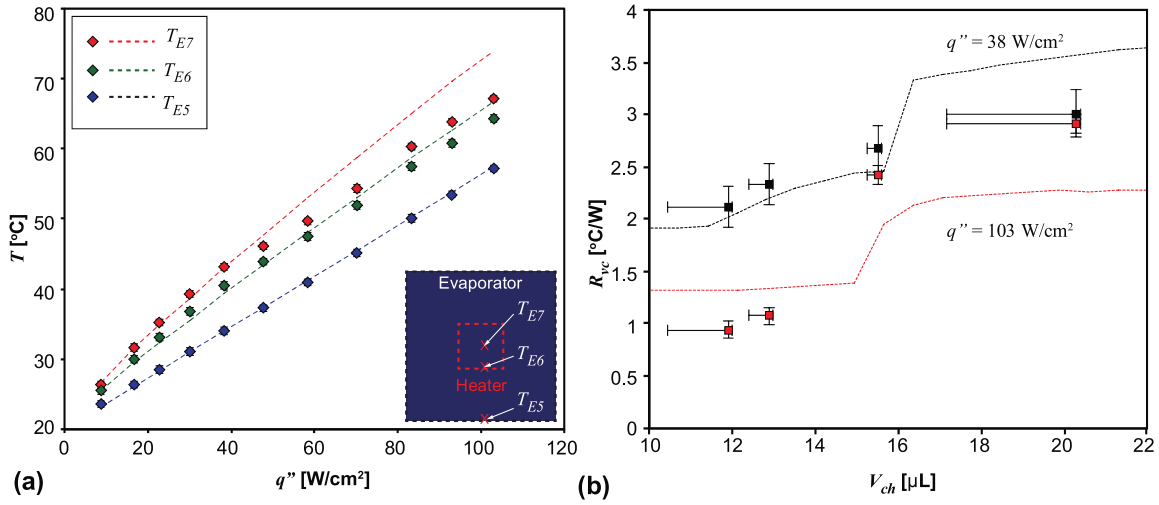

Fig. 10. (a) Experimental data and model fit for temperature profiles at three different RTD locations of T_{E7}, T_{E6}, and T_{E5} on the evaporator surface as a function of input heat flux for a liquid charge of 11.9 μL. The location of the RTDs relative to the heater and overall evaporator area are shown in the inset. (b) Experimental data and model fit for thermal resistance at two different heat fluxes of 38 W/cm^2 and 103 W/cm^2 as a function of liquid charge. A clear transition point exists at charge volumes between 15–17 μL, above which the condenser becomes flooded and the device resistance increases drastically.

mal conductivity, though the area averaged model approach still shows good agreement with experimental results within 10%.

The model results for the vapor chamber thermal resistance as a function of liquid charge is plotted for two different heat fluxes of 38 W/cm^2 and 103 W/cm^2 against the experimental results in Fig. 10(b). The resistance behavior of the vapor chamber shows a clear transition at liquid charge levels approaching a wick saturation ratio greater than 1. This is due to the formation of a flooded liquid layer on the condenser side wick that provides a significant series resistance to the overall device and creates an undesirable operational mode. The device resistance varies by approximately 0.05 °C/W/μL of liquid below the threshold value, but shows a sudden increase of around 0.5 °C/W/μL once the threshold is crossed. Proper identification of the threshold value and charging precision of at least ±2 μL around that value is therefore necessary to ensure optimal device performance. The threshold charge level also appears to shift to the left at the higher heat flux considered, as significant redistribution of liquid from the evaporator to the condenser side can cause flooding to occur at lower charge levels. The net effect on the device resistance with increasing heat flux is then the interplay between a decreasing evaporator resistance and increasing condenser resistance. The model also implies that above a certain heat flux, decreasing the liquid charge level may no longer have a significant impact on the overall device resistance. For the maximum heat flux value considered of 103 W/cm^2, increasing the charge level from 10 μL to 15 μL shows a less than 6% change in total thermal resistance. Increasing the liquid charge by the same amount at the lower heat flux of 38 W/cm^2, however, causes the resistance to increase by more than 25%. The optimal liquid charge volume will therefore also depend on the desired operational heat flux of the device.

The complete experimental data set for thermal resistance is plotted against the model prediction in Fig. 11. Overall, the model results agree with the experimental values within ±25%, though the agreement is closer for the lower levels of liquid charge. The majority of the model uncertainty comes from the uncertainty in the height of the micropillar wicks and subsequent saturated liquid charge volume. The predicted thermal resistance is particularly sensitive to the micropillar height in the flooded regime and leads to a larger model uncertainty for higher liquid charge levels, as any extra liquid film formation on the condenser side contributes a significant series resistance. This may explain some of the model discrepancy for the liquid charge volumes of 15.5 μL and 20.3 μL. The model appears to consistently underpredict the values for the higher charge volumes in the lower resistance ranges, however, which implies that the effect of increasing heat flux is not decreasing the measured resistance values as much as the model prediction. This may be due to the fact that some flooding is actually occurring in the evaporator wick with the higher liquid charge levels, and the pinned evaporator meniscus model is not applicable over the full heat flux range considered.

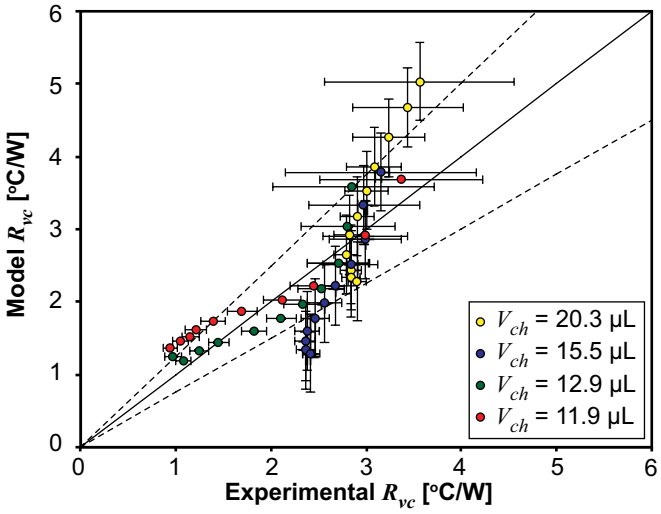

Fig. 11. Model prediction for vapor chamber thermal resistance versus all data for experimentally measured thermal resistance. Overall, model prediction agrees with experimental values within 25%, with better agreement for lower liquid charge levels.

To benchmark the miniature vapor chamber thermal performance, simulations were performed in COMSOL for two solid silicon slabs of different thicknesses with the same heating and condenser side cooling boundary conditions as the vapor chamber experiment. A direct comparison with other existing silicon vapor chambers is difficult due to the different form factors and innate spreading resistances involved. Therefore, solid silicon slabs were chosen as an appropriate baseline case to assess the potential benefit of using the miniature vapor chamber for die-level heat

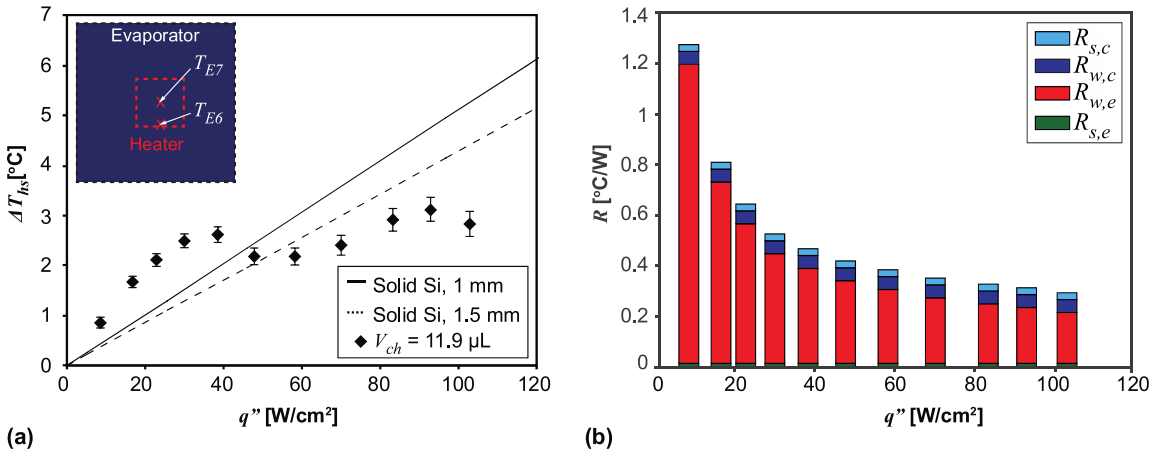

Fig. 12. (a) ΔT_{hs}, or the difference between T_{E7} and T_{E6}, as a function of heat flux for simulated solid bare silicon slabs of 1 mm and 1.5 mm thickness, respectively, compared against experimental results for a liquid charge volume of 11.9 μL. The vapor chamber shows an improvement over the solid silicon slabs for heat fluxes above 60 W/cm^2. (b) 1D resistance stack up of various vapor chamber components as a function of heat flux for modeled liquid charge volume of 11.9 μL. The evaporator wick resistance, $R_{w,e}$, is strongly dependent on heat flux and dominates compared to the solid evaporator/condenser silicon resistances, $R_{s,c}$ and $R_{s,e}$, and condenser wick resistance, $R_{w,c}$.

spreading. Fig. 12(a) compares the experimental results for the vapor chamber with 11.9 μL liquid charge for the temperature drop across the hotspot, $\Delta T_{hs,}$ defined as T_{E7} - T_{E6}, with the simulation results for solid silicon slabs of 1 mm and 1.5 mm thickness. The total vapor chamber thickness of 1.5 mm was chosen primarily for ease of fabrication to enable a one-step etch to define the vapor core, but leaves approximately 400 μm of solid silicon on the condenser side with minimal contribution to the thermal spreading performance. As the overall stack thickness can be easily reduced to 1 mm or thinner without impacting the vapor chamber performance by dividing the vapor core between the evaporator and condenser side wafers, we include the 1 mm thick solid silicon slab as a benchmark of a more realistic commercial form factor. The vapor chamber shows an improvement in hotspot temperature non-uniformity over both the 1.5 mm and 1 mm slabs of approximately 36% and 46%, respectively, at the maximum heat flux considered. At heat fluxes below 60 W/cm^2, however, the vapor chamber has no clear benefit over a solid spreader.

To investigate the origin of this threshold heat flux, we use the model to examine the various components that form the 1D resistance stack of the vapor chamber in Fig. 12(b). The evaporator wick resistance, $R_{w,e}$, dominates compared to the condenser wick resistance, $R_{w,c}$, as well as the solid silicon resistances on both sides of the device, $R_{s,e}$ and $R_{s,c}$. $R_{w,e}$ decreases with increasing heat flux due to two simultaneous effects: an increase in the thin-film area with increasing rates of evaporation, as well as a decrease in interfacial resistance with increasing temperature. At heat fluxes above 50 W/cm^2, the evaporator wick shows a diminishing dependence on heat flux and appears to approach a minimum resistance value of approximately 0.2 °C/W. This corresponds to the experimental trends observed in Fig. 12(a), where the vapor chamber appears to become more effective at heat fluxes higher than 50–60 W/cm^2. Operating at a higher condenser side temperature to decrease the interfacial resistance throughout the device would perhaps extend the effective vapor chamber range to lower heat fluxes, as would moving to an evaporator wick structure with a lower thermal resistance. The strong heat flux dependence of $R_{w,e}$ at lower heat fluxes implies that for the wick dimensions considered, the interfacial and thin-film resistances have a large contribution to the overall stack resistance. The minimum wick resistance value may ultimately be limited by the conduction resistance across the wick, however, so simultaneously moving to a higher density and thinner micropillar wick could be an effective solution to reduce the overall thermal resistance of the device and improve the low heat flux performance. A higher density and thinner wick may also potentially reduce the maximum capillary-limited heat dissipation capability of the vapor chamber, however, so careful consideration of both the thermal properties as well as fluidic transport is necessary for future design optimization.

It is clear from Fig. 12(a) that the miniature vapor chamber will have a much more significant improvement compared to a solid spreader of the same dimensions if it can be reduced to a thinner form factor. As the only high thermal conductivity portion of the vapor chamber is the vapor core, the extra silicon thickness on the condenser side in the current form factor only serves to obscure the effectiveness of the phase change region when compared to a solid spreader of equal dimensions. Reducing the overall vapor chamber thickness to 1 mm should have minimal impact on the current thermal performance, and provides a much more significant improvement over the solid silicon equivalent.

5. Conclusions

A miniature vapor chamber with an active vapor transport region of 1 × 1 cm^2 was fabricated and experimentally characterized for a range of liquid charge volumes and heat flux inputs. A model was developed to predict the impact of both heat flux and liquid charge on the vapor chamber thermal performance and experimentally validated to agree within ±25%. The model demonstrates that the liquid charge dependence of the vapor chamber resistance increases sharply near the wick saturation threshold due to the flooding of the condenser wick and creates an undesirable high thermal resistance operational mode. The evaporator wick resistance dominates the overall 1D vapor chamber resistance stack and decreases with increasing heat input. Above a certain heat flux level, however, the heat flux dependence of the wick diminishes and approaches a minimum value.

The vapor chamber thermal performance was benchmarked against simulation results for solid silicon spreaders of varying thickness. The current prototype vapor chamber thickness of 1.5 mm contains extra silicon thickness on the condenser side with minimal thermal impact that makes for a relatively ineffective comparison with an equivalent solid silicon spreader. The experimental results did demonstrate, however, that the vapor chamber shows superior temperature uniformity over a 1 mm thick solid spreader for heat fluxes greater than 50–60 W/cm^2. If the unused silicon can be removed, the vapor chamber can achieve significant improvement in thermal performance over a solid silicon spreader

of equivalent thickness and effectively improve die-level temperature uniformity over an area as small as 1×1 cm^2.

The modeling methodology developed in this work can be used to aid the design of future small-scale vapor chamber heat spreaders. The thermal performance of the vapor chamber is dependent on a number of internal as well as system design parameters, and due to the small spreading distances considered, may not always have an obvious impact over a solid spreader of equivalent dimension. Comparison of the model with experimental results elucidates the primary resistance components that dominate the vapor chamber performance, as well as the sensitivity of the vapor chamber performance to the liquid charge level. Due to the small liquid charge volume involved (on the order of microliters), this provides important guidelines to aid the process development of other future microscale devices. This work shows that there is potential benefit for vapor chambers to be implemented over spreading areas as small as 1×1 cm^2, but careful assessment of different parameters such as the desired operating heat flux range is necessary to determine whether or not such a small-scale device is beneficial.

Declaration of Competing Interest

The authors declare that they have no known competing financial interests or personal relationships that could have appeared to influence the work reported in this paper

CRediT authorship contribution statement

Tanya Liu: Methodology, Investigation, Data curation, Validation, Writing - original draft. **Marc T. Dunham:** Conceptualization, Supervision. **Ki Wook Jung:** Methodology, Resources. **Baoxing Chen:** Conceptualization, Supervision. **Mehdi Asheghi:** Conceptualization, Supervision, Project administration. **Kenneth E. Goodson:** Conceptualization, Supervision, Project administration.

Acknowledgements

This work was supported in part by Analog Devices, Inc., as well as the Semiconductor Research Corporation (SRC) and DARPA. This work was also partially supported by the U.S. National Science Foundation Engineering Research Center on Power Optimization of Electro-Thermal Systems (POETS) with cooperative agreement EEC-1449548. Part of this work was performed at the Stanford Nano Shared Facilities (SNSF)/Stanford Nanofabrication Facility (SNF), supported by NSF under Award No. ECCS-1542152. T. Liu also acknowledges support from the NSF Graduate Research Fellowship Program. Any opinions, findings, and conclusions or recommendations expressed in this material are those of the author(s) and do not necessarily reflect the views of the National Science Foundation.

Supplementary materials

Supplementary material associated with this article can be found, in the online version, at doi:10.1016/j.ijheatmasstransfer.2020.119569.

References

[1] A. Shakouri, Y. Zhang, On-chip solid-state cooling for integrated circuits using thin-film microrefrigerators, IEEE Trans. Components Packag. Technol. 28 (2005) 65–69, doi:10.1109/TCAPT.2005.843219.
[2] A. Bar-Cohen, M. Arik, M. Ohadi, Direct liquid cooling of high flux micro and nano electronic components, Proc. IEEE. 94 (2006) 1549–1570, doi:10.1109/JPROC.2006.879791.
[3] A. Bar-Cohen, K. Matin, N. Jankowski, D. Sharar, Two-Phase thermal ground planes: technology development and parametric results, J. Electron. Packag. 137 (2014) 010801, doi:10.1115/1.4028890.
[4] Y. Koito, H. Imura, M. Mochizuki, Y. Saito, S. Torii, Numerical analysis and experimental verification on thermal fluid phenomena in a vapor chamber, Appl. Therm. Eng. 26 (2006) 1669–1676, doi:10.1016/j.applthermaleng.2005.11.012.
[5] Amir Faghri, Heat Pipe Science and Technology, 2nd ed., Global Digital Press, 2016.
[6] X. Ji, J. Xu, A.M. Abanda, Copper foam based vapor chamber for high heat flux dissipation, Exp. Therm. Fluid Sci. 40 (2012) 93–102, doi:10.1016/j.expthermflusci.2012.02.004.
[7] S.C. Wong, K.C. Hsieh, J. Da Wu, W.L. Han, A novel vapor chamber and its performance, Int. J. Heat Mass Transf. 53 (2010) 2377–2384, doi:10.1016/j.ijheatmasstransfer.2010.02.001.
[8] Y. Wang, K. Vafai, An experimental investigation of the thermal performance of an asymmetrical flat plate heat pipe, Int. J. Heat Mass Transf. 43 (2000) 2657–2668, doi:10.1016/S0017-9310(99)00300-2.
[9] R. Prasher, Thermal interface materials: historical perspective, status, and future directions, Proceedings of the IEEE 94 (8) (2006) 1571–1586.
[10] U. Vadakkan, G.M. Chrysler, S. Sane, Silicon/water vapor chamber as heat spreaders for microelectronic packages, Semicond. Therm. Meas. Manag. IEEE Twenty First Annu. IEEE Symp. (2005) 182–186, doi:10.1109/stherm.2005.1412176.
[11] T. P. Cotter., Principles and prospects for micro heat pipes (No. LA-UR-84-120; CONF-840578-1). (1984) Los Alamos National Lab., NM (USA).
[12] G.P. Peterson, A.B. Duncan, M.H. Weichold, Experimental investigation of micro heat pipes fabricated in silicon wafers, J. Heat Transf. 115 (1993) 751–756.
[13] M. Le Berre, S. Launay, V. Sartre, M. Lallemand, Fabrication and experimental investigation of silicon micro heat pipes, J. Micromech. Microeng. 13 (2003) 436–441 0960-1317/13/3/313.
[14] L.L. Vasiliev, Micro and miniature heat pipes - Electronic component coolers, Appl. Therm. Eng. 28 (2008) 266–273, doi:10.1016/j.applthermaleng.2006.02.023.
[15] Q. Cai, B.C. Chen, C. Tsai, Design, development and tests of high-performance silicon vapor chamber, J. Micromech. Microeng. 22 (2012), doi:10.1088/0960-1317/22/3/035009.
[16] C. Gillot, Y. Avenas, N. Cézac, G. Poupon, C. Schaeffer, E. Fournier, Silicon heat pipes used as thermal spreaders, IEEE Transactions on Components and Packaging Technologies 26 (2) (2003) 332–339.
[17] K.S. Yang, C.C. Lin, J.C. Shyu, C.Y. Tseng, C.C. Wang, Performance and two-phase flow pattern for micro flat heat pipes, Int. J. Heat Mass Transf. 77 (2014) 1115–1123, doi:10.1016/j.ijheatmasstransfer.2014.06.056.
[18] J. Liang, M.S. Bakir, Y. Joshi, Microfabricated thin silicon vapor chamber for low profile thermal management, in: The 16th IEEE Intersociety Conference on Thermal and Thermomechanical Phenomena in Electronic Systems (ITherm), 2017, pp. 529–536, doi:10.1109/ITHERM.2017.7992519.
[19] M. Ivanova, A. Lai, C. Gillot, N. Sillon, C. Schaeffer, F. Lefèvre, M. Lallemand, E. Fournier, Design, fabrication and test of silicon heat pipes with radial microcapillary grooves, Thermomech. Phenom. Electron. Syst. -Proceedings Intersoc. Conf. (2006) 545–551, doi:10.1109/ITHERM.2006.1645392.
[20] B. He, M. Wei, S. Somasundaram, C.S. Tan, E.N. Wang, Experiments on the ultrathin silicon vapor chamber for enhanced heat transfer performance, Proc. 15th Intersoc. Conf. Therm. Thermomechanical Phenom. Electron. Syst. ITherm (2016) 569–573, doi:10.1109/ITHERM.2016.7517598.
[21] C.A. Mack, Fifty years of Moore's law, IEEE Trans. Semicond. Manuf. 24 (2011) 202–207, doi:10.1109/TSM.2010.2096437.
[22] S.W. Kang, S.H. Tsai, H.C. Chen, Fabrication and test of radial grooved micro heat pipes, Appl. Therm. Eng. 22 (2002) 1559–1568, doi:10.1016/S1359-4311(02)00085-6.
[23] Z. Ming, L. Zhongliang, M. Guoyuan, The experimental and numerical investigation of a grooved vapor chamber, Appl. Therm. Eng. 29 (2009) 422–430, doi:10.1016/j.applthermaleng.2008.03.030.
[24] C. Oshman, B. Shi, C. Li, R. Yang, Y.C. Lee, G.P. Peterson, V.M. Bright, The development of polymer-based flat heat pipes, J. Microelectromechanical Syst 20 (2011) 410–417, doi:10.1109/JMEMS.2011.2107885.
[25] R.S. Prasher, A simplified conduction based modeling scheme for design sensitivity study of thermal solution utilizing heat pipe and vapor chamber technology, J. Electron. Packag. 125 (2003) 378, doi:10.1115/1.1602479.
[26] S. Cho, Y. Joshi, Thermal performance of microelectronic substrates with sub-mm integrated vapor chamber, J. Heat Transfer 141 (2018) 1–12, doi:10.1115/1.4042328.
[27] G. Patankar, J.A. Weibel, S.V. Garimella, Patterning the condenser-side wick in ultra-thin vapor chamber heat spreaders to improve skin temperature uniformity of mobile devices, Int. J. Heat Mass Transf. 101 (2016) 927–936, doi:10.1016/j.ijheatmasstransfer.2016.05.093.
[28] G. Carbajal, C.B. Sobhan, G.P. Bud Peterson, D.T. Queheillalt, H.N.G. Wadley, A quasi-3D analysis of the thermal performance of a flat heat pipe, Int. J. Heat Mass Transf. 50 (2007) 4286–4296, doi:10.1016/j.ijheatmasstransfer.2007.01.057.
[29] U. Vadakkan, S.V. Garimella, J.Y. Murthy, Transport in flat heat pipes at high heat fluxes from multiple discrete sources, J. Heat Transfer 126 (2004) 347, doi:10.1115/1.1737773.
[30] R. Ranjan, J.Y. Murthy, S.V. Garimella, U. Vadakkan, A numerical model for transport in flat heat pipes considering wick microstructure effects, Int. J. Heat Mass Transf. 54 (2011) 153–168, doi:10.1016/j.ijheatmasstransfer.2010.09.057.
[31] A.J. Jiao, H.B. Ma, J.K. Critser, Evaporation heat transfer characteristics of a grooved heat pipe with micro-trapezoidal grooves, Int. J. Heat Mass Transf. 50 (2007) 2905–2911, doi:10.1016/j.ijheatmasstransfer.2007.01.009.

[32] F. Lefèvre, R. Rullière, G. Pandraud, M. Lallemand, Prediction of the temperature field in flat plate heat pipes with micro-grooves - Experimental validation, Int. J. Heat Mass Transf. 51 (2008) 4083–4094, doi:10.1016/j.ijheatmasstransfer.2007.12.007.
[33] K.H. Do, S.J. Kim, S.V. Garimella, A mathematical model for analyzing the thermal characteristics of a flat micro heat pipe with a grooved wick, Int. J. Heat Mass Transf. 51 (2008) 4637–4650, doi:10.1016/j.ijheatmasstransfer.2008.02.039.
[34] Y. Zhu, D.S. Antao, Z. Lu, S. Somasundaram, T. Zhang, E.N. Wang, Prediction and characterization of dry-out heat flux in micropillar wick structures, Langmuir 32 (2016) 1920–1927, doi:10.1021/acs.langmuir.5b04502.
[35] D. Ćoso, V. Srinivasan, M.-.C. Lu, J.-.Y. Chang, A. Majumdar, Enhanced heat transfer in biporous wicks in the thin liquid film evaporation and boiling regimes, J. Heat Transfer 134 (2012) 101501, doi:10.1115/1.4006106.
[36] S. Adera, D. Antao, R. Raj, E.N. Wang, Design of micropillar wicks for thin-film evaporation, Int. J. Heat Mass Transf. 101 (2016) 280–294, doi:10.1016/j.ijheatmasstransfer.2016.04.107.
[37] R. Ranjan, J.Y. Murthy, S.V. Garimella, Analysis of the wicking and thin-film evaporation characteristics of microstructures, J. Heat Transfer 131 (2009) 101001, doi:10.1115/1.3160538.
[38] H. Wang, S.V. Garimella, J.Y. Murthy, Characteristics of an evaporating thin film in a microchannel, Int. J. Heat Mass Transf. 50 (2007) 3933–3942, doi:10.1016/j.ijheatmasstransfer.2007.01.052.
[39] H.B. Ma, P. Cheng, B. Borgmeyer, Y.X. Wang, Fluid flow and heat transfer in the evaporating thin film region, Microfluid. Nanofluidics. 4 (2008) 237–243, doi:10.1007/s10404-007-0172-5.
[40] P.C. Stephan, C.A. Busse, Analysis of the heat transfer coefficient of grooved heat pipe evaporator walls, Int. J. Heat Mass Transf. 35 (1992) 383–391, doi:10.1016/0017-9310(92)90276-X.
[41] R. Ranjan, J.Y. Murthy, S.V. Garimella, A microscale model for thin-film evaporation in capillary wick structures, Int. J. Heat Mass Transf. 54 (2011) 169–179, doi:10.1016/j.ijheatmasstransfer.2010.09.037.
[42] V.P. Carey, Liquid-Vapor Phase-Change Phenomena: An Introduction to the Thermophysics of Vaporization and Condensation Processes in Heat Transfer Equipment, 2nd Edition, 2008.
[43] L.E. Scriven, C.V. Sternling, The marangoni effects, Nature 187 (4733) (1960) 186–188.
[44] J.B. Boreyko, C.H. Chen, Vapor chambers with jumping-drop liquid return from superhydrophobic condensers, Int. J. Heat Mass Transf. 61 (2013) 409–418, doi:10.1016/j.ijheatmasstransfer.2013.01.077.
[45] L.D. Eske, D.W. Galipeau, Characterization of sio2 surface treatments using AFM, contact angles and a novel dewpoint technique, Colloids Surfaces A Physicochem. Eng. Asp. 154 (1999) 33–51, doi:10.1016/S0927-7757(98)00907-8.
[46] C. Byon, S.J. Kim, The effect of meniscus on the permeability of micro-post arrays, J. Micromech. Microeng. (2011) 21, doi:10.1088/0960-1317/21/11/115011.
[47] G. Patankar, J.A. Weibel, S.V. Garimella, Working-fluid selection for minimized thermal resistance in ultra-thin vapor chambers, Int. J. Heat Mass Transf. 106 (2017) 648–654, doi:10.1016/j.ijheatmasstransfer.2016.09.038.
[48] Y.S. Muzychka, Influence coefficient method for calculating discrete heat source temperature on finite convectively cooled substrates, IEEE Trans. Compon. Packag. Technol. 29 (2006) 636–643, doi:10.1109/TCAPT.2006.880477.
[49] J.H. Lienhard, L. Lienhard, A Heat Transfer Textbook, 4th Edition, Dover, 2018.